

Published in final edited form as:

*Nat Mater.* 2019 May 8; 18(8): 853–859. doi:10.1038/s41563-019-0382-8.

## Quantitative imaging of electric surface potentials with single-atom sensitivity

Christian Wagner<sup>1,2,\*</sup>, Matthew F. B. Green<sup>1,2,3</sup>, Michael Maiworm<sup>4</sup>, Philipp Leinen<sup>1,2,3</sup>,  
Taner Esat<sup>1,2,3</sup>, Nicola Ferri<sup>5</sup>, Niklas Friedrich<sup>1,2,3</sup>, Rolf Findeisen<sup>4</sup>, Alexandre  
Tkatchenko<sup>5,6</sup>, Ruslan Temirov<sup>1,2,7</sup>, F. Stefan Tautz<sup>1,2,3</sup>

<sup>1</sup>Peter Grünberg Institut (PGI-3), Forschungszentrum Jülich, 52425 Jülich, Germany

<sup>2</sup>Jülich Aachen Research Alliance (JARA)-Fundamentals of Future Information Technology, 52425 Jülich, Germany

<sup>3</sup>Experimentalphysik IV A, RWTH Aachen University, Otto-Blumenthal-Straße, 52074 Aachen, Germany

<sup>4</sup>Otto-von-Guericke-Universität Magdeburg, Laboratory for Systems Theory and Automatic Control, Magdeburg, Germany

<sup>5</sup>Fritz-Haber-Institut der Max-Planck-Gesellschaft, Faradayweg 4-6, 14195, Berlin, Germany

<sup>6</sup>Physics and Materials Science Research Unit, University of Luxembourg, 1511 Luxembourg, Luxembourg

<sup>7</sup>II. Physikalisches Institut, Universität zu Köln, Zùlpicher Straße 77, 50937 Köln, Germany

### Abstract

Because materials consist of positive nuclei and negative electrons, electric potentials are omnipresent at the atomic scale. However, due to the long range of the Coulomb interaction, large-scale structures completely outshine small ones. This makes the isolation and quantification of the electric potentials that originate from nanoscale objects such as atoms or molecules very challenging. Here we report a noncontact scanning probe technique which addresses this challenge. It exploits a quantum dot sensor and the joint electrostatic screening by tip and surface, thus enabling quantitative surface potential imaging across all relevant length scales down to single atoms. We apply the technique to the characterization of a nanostructured surface, thereby

---

Users may view, print, copy, and download text and data-mine the content in such documents, for the purposes of academic research, subject always to the full Conditions of use:[http://www.nature.com/authors/editorial\\_policies/license.html#terms](http://www.nature.com/authors/editorial_policies/license.html#terms)

\*Correspondence and requests for materials should be addressed to C.W. [c.wagner@fz-juelich.de](mailto:c.wagner@fz-juelich.de).

**Code availability** The custom code that was used for the deconvolution in this study is available from the corresponding author upon reasonable request.

#### Author contributions

C.W., R.T. and F.S.T. conceived and designed this research. M.F.B.G., P.L., T.E., N.Fr. and M.M. performed the experiments, C.W. and M.F.B.G. analysed the data. M.M. and R.F. designed and provided the feedback controller, N.Fe. and A.T. conducted the DFT simulations. C.W. and F.S.T. interpreted the data, developed the theory of SQDM imaging and wrote the paper.

#### Additional information

Reprints and permissions information is available online at [www.nature.com/reprints](http://www.nature.com/reprints).

#### Competing financial interests

The authors declare no competing financial interests.

extracting work function changes and dipole moments for important reference systems. This authenticates the method as a versatile tool to study the building blocks of materials and devices down to the atomic scale.

---

Electrostatic interactions are a key element in the functionality of many nanoscale materials and systems. For example, the performance of organic and inorganic semiconductor devices is affected by electric dipoles at the relevant interfaces [1–4]. Since both, established and novel device concepts aim for the few-nanometre scale [5–8], the relevance of microscopic electric potentials in functional materials and devices increases continually. On a more fundamental level, the measurement of electric potentials can also give valuable insights into primary mechanisms at surfaces and interfaces, such as reconstruction or relaxation, mechanical distortion, charge transfer and chemical interaction [9], which all create electric potentials at the atomic scale. But the importance of electrostatic interactions is not limited to semiconductor and solid state materials. Also the structure and aggregation of biomolecules, for example, is steered by the interactions between polarized functional groups [10, 11], and electrostatic interactions play an important role in catalysis, too [12].

In many contexts, surfaces are the natural environment to study nanoscale electric potentials, either because of their intrinsic importance (semiconductor devices, catalysis), or because they offer a convenient substrate for immobilisation and accessibility (biomolecules). The state of the art in electric potential imaging at surfaces is Kelvin Probe Force Microscopy (KPFM). KPFM is suitable for structure sizes of several tens of nanometres [4, 13–16]. For smaller structures, in the realm of single atoms or molecules [17] and cutting-edge semiconductor devices [5], KPFM is problematic since high resolution can only be reached at small tip-surface distances where chemical forces start acting. Their influence hampers a quantitative interpretation of the data [18]. KPFM images with sub-molecular resolution obtained with carbon-monoxide-decorated tips [19, 20] suffer from the same limitation, notwithstanding continuous efforts to improve the data analysis [20, 21], and are moreover slow and limited to small surface areas (typically one single molecule). Thus, a versatile, fast and quantifiable scanning probe method for imaging electric potentials at the atomic scale is lacking.

Recently we reported that a single molecule, when attached to the tip of a non-contact atomic force / scanning tunnelling microscope (NC-AFM/STM) by controlled manipulation [22, 23], may act as a quantum dot (QD) and can be used as a sensor to detect and image electric potentials, resulting in scanning quantum dot microscopy (SQDM) [24, 25]. Here, we present a rigorous analysis of the corresponding imaging mechanism and show that SQDM can be used to map out surface potential distributions and dielectric surface topographies quantitatively. Most notably, we find that the screening action of the combined tip/surface system induces an exponential decay of electric potentials with lateral distance from the probing tip. This effect occasions the exceptionally high lateral resolution of SQDM. A detailed investigation of this exponential screening leads us to an image deconvolution algorithm which, in conjunction with far-reaching instrumental developments [26], transforms SQDM into a powerful imaging technique for electric surface potential imaging in ever smaller nanostructures and novel materials.

## Principle and Formalism of SQDM imaging

A schematic drawing of the molecular QD at the tip apex of a NC-AFM/STM is shown in Fig. 1a [24, 25]. This setup can be considered as a single-electron box consisting of two capacitances in series [27], but it can also be understood as an electrostatic boundary value problem where the potential  $\Phi_{\text{QD}}$  at the QD at  $r$  is determined by the shape of the confining boundary  $\mathcal{T}$  (the conductive surfaces of tip and sample connected at infinity; Fig. 1c) and by the potential distribution  $\Phi_s(r')$  on it.

It is the principle of SQDM to compensate the local variations of  $\Phi_s$  and of the sample topography beneath the QD encountered during scanning by adjusting (and recording) the sample bias  $V_b$ . The condition  $\Phi_{\text{QD}} = \text{const}$  indicates a correct compensation. This does not put special requirements on the choice of the QD and on its theoretical description. Hence, we may use the approximation of a point-like QD. Since compensation is verified at  $r$ , this is the point where the influence of the surface potential is measured. We can relate the information in this *imaging plane* back to the properties of the surface itself by defining a specific  $\mathcal{T}$  which approximates the experimental situation and solving the corresponding boundary value problem. For Dirichlet boundary conditions we obtain [28]

$$\Phi_{\text{QD}}(r) = -\frac{\epsilon_0}{e} \left[ \iint_{\text{sample}} (\Phi_s(r') + V_b) \frac{\partial G(r, r')}{\partial n'} d^2 r' + \iint_{\text{tip}} \Phi_s(r+R) \frac{\partial G(r, r+R)}{\partial n'} d^2 R \right], \quad (1)$$

while we discuss the case of non-conductive surfaces elsewhere [29]. Here,  $n'$  is the surface normal at  $r'$  or  $r+R$ , respectively, and  $G$  is the Green's function which encodes the boundary shape via  $G(r, r') = 0 \forall r' \in \mathcal{T}$  (Fig. 1c). All adsorbate-related charges which are slightly inside the volume enclosed by  $\mathcal{T}$  create, together with their image charges, the locally varying surface potential  $\Phi_s$  in Eq. 1. Since tip and QD have a fixed spatial relation and are sufficiently far from the sample, we can assume that  $G(r, r+R)/n'$  barely varies with  $r$  (during scanning) and consequently the second integral in Eq. 1 is a constant  $\Phi_T$ . Thus, from now on,  $\Phi_s$  refers to the sample surface potential only and we describe the shape of  $\mathcal{T}$  on the sample side as a topography of height  $t_d$  superimposed onto a plane such that  $r = (r_{\parallel}, z)$  and  $r' = (r'_{\parallel}, t_d)$ .

Eq. 1 is central since it relates data on  $\Phi_{\text{QD}}$  in the imaging plane at  $z$  to the desired surface properties. For a chosen shape of  $\mathcal{T}$ ,  $\Phi_s(r'_{\parallel})$  as calculated by inversion of Eq. 1 corresponds to the potential distribution which, if applied to  $\mathcal{T}$ , would reproduce the  $\Phi_{\text{QD}}$  data in the imaging plane. Thus, a more accurate representation of  $\mathcal{T}$  yields a better recovery of  $\Phi_s(r'_{\parallel})$ .

As it turns out, the approximation of a planar surface with  $t_d = 0$ , which we will adopt in the following, provides excellent results for the systems investigated here, where generally  $t_d \ll z$ . A discussion of alternative approximations for  $t_d$  and their consequences is given in Ref. [29]. Moreover, we adopt the reasonable assumption of an axially symmetric tip.

For these conditions,  $G/n'$  depends only on the relative distance  $|r_{\parallel} - r'_{\parallel}|$  and is the point spread function (PSF)  $\gamma(|r_{\parallel} - r'_{\parallel}|, z) \equiv -\epsilon_0 / e \times \partial G / \partial n'$  of SQDM (Fig. 1d). Then, Eq. 1 becomes (from now on we drop the explicit reference to  $z$ )

$$\Phi_{\text{QD}}(r_{\parallel}) = (V^*(r_{\parallel}) + V_b)\alpha(r_{\parallel}) + \Phi_T \quad (2)$$

with the following definitions for  $\alpha$  and  $V^*$

$$\alpha(r_{\parallel}) = \iint_{\text{sample}} \gamma(|r_{\parallel} - r'_{\parallel}|) d^2 r'_{\parallel} = \frac{\partial \Phi_{\text{QD}}}{\partial V_b} \quad (3)$$

$$V^*(r_{\parallel}) = \iint_{\text{sample}} \Phi_s(r'_{\parallel}) \gamma^*(|r_{\parallel} - r'_{\parallel}|) d^2 r'_{\parallel} \quad (4)$$

Analogous equations can be derived for a more general  $\mathcal{F}$  with  $t_d = 0$  [29]. Here,  $\alpha$  is the gating efficiency,  $\gamma^* = \gamma/\alpha$  is the PSF normalized to one, and  $V^*$  quantifies the effect of the surface potential distribution  $\Phi_s$  on  $\Phi_{\text{QD}}$  expressed in the form of an equivalent (additional) bias potential. For extended, homogeneous objects with constant  $\Phi_s$ ,  $V^*$  is in fact the surface potential:  $\Phi_s = V^*$ . Inhomogeneous potential distributions  $\Phi_s(r'_{\parallel})$  can be obtained from  $V^*$  via a deconvolution with the PSF  $\gamma^*$  (Eq. 4) as we will discuss later. First we demonstrate how  $\alpha$  and  $V^*$  can be extracted from an actual SQDM measurement.

At two specific  $\Phi_{\text{QD}}$  values  $\Phi^+$  and  $\Phi^-$  the QD charge state changes as an electron tunnels across the contact between tip and QD [24]. These charging events cause sharp drops in the frequency shift  $f(V_b)$  of the NC-AFM (Fig. 1b), corresponding to steps in the tip-surface force [30, 31]. These drops at  $V_b = V^{\pm}(r_{\parallel})$  are indicators that the charging condition  $\Phi_{\text{QD}} = \Phi^{\pm}$  has been reached and that the compensation of  $V^*$  was hence successful. Thus,  $V^{\pm}$  are the primary measurands of SQDM. To image  $V^{\pm}$ , we have developed a feedback controller which maintains the charging condition either for  $V^+$  or for  $V^-$  as the surface is scanned twice at constant height [26] (see Methods).

After some algebra we can derive the following two relations from Eq. 2 and the charging conditions:

$$\alpha_{\text{rel}}(r_{\parallel}) = \frac{\alpha(r_{\parallel})}{\alpha_0} = \frac{V_0^+ - V_0^-}{V^+(r_{\parallel}) - V^-(r_{\parallel})} \quad (5)$$

and

$$V^*(r_{\parallel}) = \frac{V_0^-}{\alpha_{\text{rel}}(r_{\parallel})} - V^-(r_{\parallel}). \quad (6)$$

Since SQDM measures *variations* in  $\Phi_s$  and  $\alpha$ , we have selected a reference point on the surface where we define  $z$ ,  $\Phi_s \equiv 0$ ,  $\alpha \equiv \alpha_0$ , and denote the measured  $V^{\pm}$  values as  $V_0^{\pm}$ . With this, we have established  $V^*(r_{\parallel})$  and  $\alpha_{\text{rel}}(r_{\parallel})$  as the secondary SQDM measurands. Note that the absolute value of  $\alpha$  can be determined from  $V^{\pm}(z)$  and corresponding force change datasets [32], which is, however, not required for SQDM.

## Measuring work function changes

We demonstrate the quantitative measurement of the surface potential  $\Phi_s$  for a homogeneous sample by looking at work function changes. The corresponding experiment was carried out on PTCDA (3,4,9,10-perylene-tetracarboxylic dianhydride) adsorbed on the Ag(111) surface with a PTCDA molecule as SQDM sensor [24, 25] using a qPlus NC-AFM. Although PTCDA/Ag(111) is an extremely well-studied benchmark system [33], no consensus has yet been reached regarding the work function change  $W$  upon adsorption of PTCDA on Ag(111). In fact, values between  $-0.1$  eV and  $+0.27$  eV have been reported from photoemission experiments [34–36] (black squares in Fig. 1e). In Fig. 1e we show line profiles of  $V^*$ , measured from the bare Ag(111) surface across PTCDA island edges deep into a compact PTCDA island for different tip preparations, tip heights, and even different NC-AFM tuning forks. Remarkably, the line scans collapse practically onto a single curve, proving that work function changes as determined by SQDM are robust and reproducible, and yield a value of  $W = -e\Phi_s = -eV^* = (145 \pm 10)$  meV from Ag(111) to PTCDA/Ag(111).

We compare the work function determined by SQDM to results obtained from density functional theory (DFT) calculations. We employ a fully self-consistent implementation,  $\text{vdW}_{\text{sc}}^{\text{surf}}$  [37], of the Tkatchenko-Scheffler  $\text{vdW}_{\text{sc}}^{\text{surf}}$  functional [38], in combination with PBE [39] (see Methods). The calculated work function shift between Ag(111) and PTCDA/Ag(111) is  $W = 90$  meV. Compared to PBE, which predicts a value of 240 meV,  $\text{vdW}_{\text{sc}}^{\text{surf}}$  yields an improved though not perfect agreement with the experimental value. This result stresses the fundamental importance of van der Waals interactions for electronic processes at molecule/metal interfaces and, on a more general note, shows that SQDM is able to set benchmarks for the development of ab-initio theory.

Turning back to the experiment, the curves in Fig. 1e also reveal the sharpness with which we measure the potential distribution at the island edge. To put our experimental  $V^*(r_{\parallel})$  curve into perspective, we compare it with two extreme cases: First, a simulated estimate for a corresponding classical KPFM experiment [13] (grey solid curve) in which the entire tip acts as a sensor for the electric potential, and second, a simulation of the measurement with an idealized hypothetical point-like sensor for electrostatic potentials (red dotted curve in Fig. 1e, compare also Fig. 2a). While it is expected that the  $V^*$  resolution of SQDM,

because of its nanoscopic sensor, is superior to KPFM, the profile we observe in experiment is even sharper than that of the 'ideal' point probe. This surprising finding asks for a closer analysis of the physics behind the PSF  $\gamma^*$  which, according to Eq. 4, determines how a step in the surface potential  $\Phi_s$  is smeared into  $V^*$ . Knowing  $\gamma^*$  will ultimately allow the reconstruction of arbitrary potential distributions  $\Phi_s(r_{||})$  via Eq. 4.

## The functional form of $\gamma^*$ and image deconvolution

To analyse the shape of  $\gamma^*$ , we must solve the boundary value problem for the chosen shape of  $\mathcal{T}$ . To reach a generic solution, we approximate also the tip as planar which is justified since the PtIr tips used in our experiments are rather blunt on the mesoscopic scale, which is also confirmed by our experimental results. Other tip shapes would not invalidate the general conclusions drawn here [29].

For Dirichlet conditions, the gradient  $\partial G(r_{||}, r'_{||})/\partial n'$  and thus  $\gamma^*$  is proportional to the potential at  $r_{||}$  of a test charge placed at  $r'_{||}$  and shifted slightly into the volume enclosed by the grounded surface  $\mathcal{T}$ , which creates a minimal perturbation of  $\Phi_s(r_{||})$ . The respective  $\gamma_{pp}^*$  for grounded parallel planes separated by  $z_t = z+d$  can then be calculated via an infinite series of image charges (Fig. 2c) which screen the test charge placed at  $(r'_{||} = 0, z_c \ll z)$ . This series has no closed solution [40], but there exists an asymptotic expression for large  $r_{||}$  that clearly reveals an (even faster than) exponential decay of  $\gamma_{pp}^*$  with  $|r_{||}|$  [41]

$$\gamma_{pp}^*(|r_{||}|, z, z_t) \propto \sqrt{\frac{8}{|r_{||}|z_t}} \sin\left(\frac{z}{z_t}\pi\right) \sin\left(\frac{z_c}{z_t}\pi\right) e^{-\frac{\pi}{z_t}|r_{||}|}. \quad (7)$$

To put this result into perspective, we compare it with the PSF of a hypothetical ideal point probe (instead of tip and QD) (Fig. 2a) which behaves as  $p \cdot \hat{r}/r^2$  (Fig. 2b), as expected for the test-charge/image-charge dipole.

The exponential decay of the PSF  $\gamma^*$  (which is not exclusive to the parallel-plane approximation) puts the sensing of electrostatic potentials via SQDM in line with STM, for which the tunnelling probability also decays exponentially with distance. In both cases the result is a superior lateral resolution, since the influence of objects which are not right beneath the probe is strongly suppressed (compare Figs. 2g and h). Remarkably, in SQDM this is achieved in spite of the long range of electrostatic fields, while the tunnelling in STM is intrinsically short-ranged. Perpendicular to the surface there is, however, no exponential decay in SQDM. This preserves its superior sensitivity at large tip heights. Beyond the tip height dependence (Eq. 7),  $\gamma^*$  depends only weakly on details of the tip. If anything, blunter tips yield a higher resolution, since their screening is stronger. This is in marked contrast to KPFM [42]. Knowing  $\gamma_{pp}^*$ , we can now obtain  $\Phi_s$  by a deconvolution of  $V^*$  (Eqs. 4 and 6, Fig. 2e, f, i, see Methods).

The second SQDM measurement quantity  $\alpha_{\text{rel}}$  (Eq. 5) is not related to  $\Phi_s$  but to the shape of  $\mathcal{F}$  via Eq. 3. Considerations summarized in the Methods and detailed in Ref. [29] show that the *dielectric topography*  $t_d(r_{\parallel})$  can be obtained from  $\alpha_{\text{rel}}(r_{\parallel})$  via deconvolution, in the same way as  $\Phi_s$  is obtained from  $V^*$ .

## An example image and its interpretation

We demonstrate the quantitative imaging of electric surface potentials and dielectric topography for a Ag(111) surface on which Ag adatoms, CO molecules and PTCDA molecules have been deposited. As the STM image Fig. 3a reveals, the surface (in a manner of speaking a 'nanotechnology construction site') contains various types of nanostructures: CO molecules, AgCO complexes, subsurface defects, a compact PTCDA monolayer, Ag adatoms on the PTCDA layer, and PTCDA-Ag<sub>2</sub> complexes that were made by controlled manipulation [43].

The surface potential  $\Phi_s$  obtained by deconvolution (Fig. 3b) reveals a rich electrostatic landscape in which all features of the STM image appear as sources of complex patterns. Particularly remarkable is the deeply structured edge of the PTCDA island, and even inside the PTCDA layer a regular pattern is discernible. The fringes and granular structures are deconvolution artefacts which arise since deconvolution is an ill-posed problem. Note that the colour scale in Fig. 3b,d is calibrated as the surface potential  $\Phi_s$ , as the work function change  $W$ , and as the surface dipole density  $\Pi_{\perp}$ , all measured relative to the bare Ag surface. The three quantities are related straightforwardly by  $W = -e\Phi_s = -e\Pi_{\perp}/\epsilon_0$ , where the second equality is the Helmholtz equation [44].

The surface potential of individual objects in Fig. 3d reveals, in addition to the vertical dipole density  $\Pi_{\perp}$  that is colour-coded, lateral multipoles such as the quadrupole moment of PTCDA and the dipole moment of PTCDA-Ag<sub>2</sub>. Evidently, this information that is not available from STM helps with the identification of nanoscale objects. Their identification is further supported by the dielectric topography in Fig. 3c. We note that the dielectric topography of all nanostructures has the same sign as in the STM image (protrusion or depression compared to bare Ag(111)). This confirms our interpretation of  $t_d$  as a (dielectric) topography. In fact, the absence of a topographic signal for certain defects allows us to classify them as subsurface defects which by their electric potential (clearly imaged in Fig. 3b) scatter surface state electrons (as obvious from Fig. 3a). We also note the appearance of CO molecules as depressions in the dielectric topography image. This is a direct consequence of the push-back effect by which the molecule depletes the spill-out electron density of the metal substrate. The dielectric topography, as well as the surface potential, also show a number of small adsorbates on the edge of the PTCDA island that are barely visible in the STM image.

On the basis of high resolution images such as the ones in Fig. 3d we have calculated surface dipole moments  $P_{\perp}$  of individual nanostructures by two-dimensional integration. The results are shown in Fig. 4a. We find that adsorption of CO on Ag(111) increases the dipole of CO to 0.75 D beyond its gas-phase value of 0.12 D, while CO adsorption on an Ag adatom on Ag(111) (which itself has a dipole of 0.66 D) results in a complex with a dipole moment of



1.65 D. The large positive dipole for the AgCO complex is of particular relevance, because this structure comes very close to the situation when a CO molecule is attached to the apex of an SPM tip, a common method to enhance image resolution [45, 46]. It has been conjectured before that the dipole of this CO-functionalized tip plays a crucial role for the correct interpretation of the corresponding images [21, 47–49]. Here we report a measurement of the dipole moment in a situation that closely resembles the adsorption of CO on the exposed tip apex. Another interesting effect in Fig. 4a is the depolarization of the PTCDA surface dipole once a molecular island is formed. The interaction between the parallel dipoles leads to a mutual reduction from -0.65 D for an isolated PTCDA molecule to -0.45 D as the intermolecular distance is decreased to  $\approx 1$  nm.

Dipoles that are created by an adsorbate on a metal surface result from a delicate interplay between the original charge distribution in the adsorbate, (de)polarization effects, charge transfers and the deformation of the metal charge density. Their measurement thus provides a sensitive benchmark to validate our ability to describe these processes quantitatively. Therefore, we compare our experimental results with DFT simulations. The dipoles computed with the PBE+vdW<sub>sc</sub><sup>surf</sup> functional for CO, the Ag adatom and the AgCO complex, adsorbed on Ag(111), are -0.30 D, +0.70 D and +1.66 D, respectively, in good overall agreement with experiment, with the well-known exception of CO [50, 51].

The close-up image in Fig. 4b reveals a modulation of the surface potential  $\Phi_s$  above the PTCDA island. Its periodicity of 1.7 nm matches the arrangement of inequivalent molecules in the PTCDA/Ag(111) unit cell. In the STM image in Fig. 3a the inequivalent molecules appear with different brightnesses. From scanning tunnelling spectroscopy it is known that charge transfer upon adsorption into the LUMO (Lowest Unoccupied Molecular Orbital) is smaller for the bright molecule than for the dark one [52]. However, since it is also known that the brighter molecule adsorbs at a larger height above the surface [53], it is not clear which of the two has the larger dipole in the end (a larger charge transfer has the tendency to increase the charge transfer dipole, but so does a larger adsorption height, which moreover will lead to a smaller pushback dipole of opposite direction). The line profile and the lateral grid in Fig. 4b reveal that the bright molecule has a lower inward pointing dipole density than the dark one. This shows that the charge transfer dipole at the PTCDA/Ag(111) interface is stronger than the push-back dipole, and that the larger charge transfer into the dark molecule overcompensates the effect of its smaller adsorption height.

A further striking feature of the PTCDA island is the strong modulation of the surface potential at its boundary. Comparing to a real-space model of the molecular layer, we can assign this structure to the uncompensated quadrupoles of PTCDA at the border where molecules alternately expose positively (hydrogen) or negatively (oxygen) charged groups. This strong electrostatic corrugation is an important reason for the preferential adsorption of small contaminants at the island edges, as found in Fig. 3.

## Outlook

SQDM offers a fresh way to look at the nanoscale world. The formalism of SQDM, based on a Dirichlet boundary value problem, is now fully clarified. We illustrate the power of the



method by presenting work function, surface dipole and electric potential measurements. A dedicated SQDM controller simplifies the recording of SQDM images to a point where SQDM requires no more effort than other atomic resolution scanning probe techniques. SQDM with a PTCDA quantum dot can easily be applied to other materials like NaCl which can be prepared with sub monolayer coverage on Ag [54] (see Supplementary Information). An even wider range of applications can be reached through the use of quantum dots that are lithographically fabricated at the end of the tip. The large tip-surface separations at which SQDM can operate make it particularly promising also for the study of rough surfaces or, for example, biomolecules with a distinct 3D structure.

## Methods

### SQDM Controller

SQDM imaging requires two images ( $V^+$  and  $V^-$ ) of the same sample area to be recorded one after another (compare Fig. 1b). We developed and used two different types of controllers for SQDM which both provide a voltage  $V$  that is added to  $V_b$  to track and compensate the changes in  $V^+$  or  $V^-$  as the tip scans the surface. Both were implemented on a commercial rapid control prototyping hardware from dSPACE GmbH. They are two-degree-of-freedom (2DOF) controllers with a feedback and a feedforward (FF) part which mainly differ in the type of the tracked feature of each  $f$  dip. For the first 2DOF controller, the feedback part is an extremum seeking controller (ESC) [55] tracking the minimum in  $f$  ( $V_b + V$ ), while the second controller is an integral controller which tracks a specific  $f$  value at the slope of each peak (slope tracking controller, STC).

The ESC computes the derivative  $d f/d V_b$  via a small modulation of  $V_b$  with a frequency  $f_{\text{mod}}$  and adjusts  $V$  such that the derivative remains zero. The advantage of this controller is its robustness. The disadvantage is its slower speed since the small  $f$  detection bandwidth requires  $f_{\text{mod}}$  to be equally small. The STC tracks a  $f$  reference value on the slope of the dip and uses the  $f$  deviation from this reference as the error signal to an integral controller. It is significantly faster than the ESC but could potentially introduce small systematic errors when the dips change their position on a non-constant background (Kelvin parabola). In the experiments presented here this error was, however, estimated to be below 1 mV.

In order to maximize the scanning speed, the FF part of both controllers uses the previous scan line as a reference for the current line. In this way, the feedback controller has to regulate only the difference between the previous and the current line to zero. Since at least one scan line (the reference) has to be acquired without the FF and thus more slowly, the scan speed can be adjusted during image acquisition. Using the STC, the total acquisition time of the  $V^\pm$  image information for Fig. 3 was two hours. More details on the 2DOF are given elsewhere [26].

### DFT simulations

All the calculations presented in this work are obtained with a fully self-consistent implementation of the Tkatchenko-Scheffler  $\text{vdW}_{\text{sc}}^{\text{surf}}$  functional [37], in combination with PBE in the full-potential all-electron code FHI-aims. The metal surfaces presented in this

work are built with six Ag layers. A vacuum of 60 Å is used in order to prevent spurious interactions between periodic images. We used a (6 × 6) unit cell with a total number of 216 silver atoms. The molecule/atom is placed in the centre. Several unit cells have been tested, the one that we employ prevents any spurious lateral interaction. During the relaxation the topmost metal layer and the molecule were allowed to relax. We set the convergence criterion to 0.01 eVÅ<sup>-1</sup> for the maximum force and employ a Monkhorst-Pack grid of (2 × 2 × 1). The energy calculations are performed with a grid of (4 × 4 × 1) k-points. We use a radius of 5 Å for the cut-off potential to ensure an accurate treatment of long-ranged vdW interactions. For all calculations, we set a convergence criteria of 10<sup>-5</sup> electrons for the electron density, 10<sup>-6</sup> eV for the total energy and 10<sup>-3</sup> eV for the sum of eigenvalues. Our calculations include scalar relativistic effects via the scaled zeroth-order regular approximation (ZORA).

The value of the dipole is linked to the change in electron density due to molecular adsorption. First, we compute the induced electron density as a function of  $z$ . This is the (2D integrated) difference between the electron density of the whole system and the densities of the isolated components, that is the metallic surface and the molecule/atom. Second, the delocalized charge is defined as the integral of the induced density along the  $z$ -axis. Finally, the change in the potential energy is computed with a second integration along the same direction. In other words, the induced dipole is obtained by solving the 1D Poisson equation along the  $z$ -direction.

### Dielectric topography

To analyze variations in  $\alpha_{\text{rel}}$ , we drop the assumption of a planar surface. Recalling the boundary value problem, topographic features in the region around  $r'$  affect the screening of the test charge (at  $r'$ ) and thus its potential at  $r$ , which is proportional to  $\gamma$ . For example, more material around  $r'$  (if  $r'$  itself is in a depression) increases the screening and thus decreases  $\gamma$  (Fig. 1c). Since the screening depends on the given material's polarizability, dielectric nanostructures screen more weakly than metallic ones. Because modifications of the substrate's metallic charge density by an adsorbate are effectively modifications in the metallic topography, they must be added to the screening effect of the (typically dielectric) adsorbate itself. Adsorbates which push back the metal charge density could thus effectively appear as depressions as it is reported for CO molecules in Fig. 3c. Leaking of metallic charge into the adsorbate via hybridization has the opposite effect. We lump all screening effects, originating from variations in real topography and dielectric properties, into a single *dielectric topography*  $t_d$  which equals the effective metallic surface topography that would cause the observed variations in  $\alpha_{\text{rel}}$ . To obtain  $t_d$  from  $\alpha_{\text{rel}}$ , we need to analyse the properties of  $\gamma$  (Eq. 3).

The non-local screening of the test charge makes  $\gamma(r_{\parallel}, r'_{\parallel})$  a functional of  $t_d(r'_{\parallel})$  which depends on  $t_d$  in an entire region of the surface. Here, we disregard this aspect, while a comprehensive analysis is given elsewhere [29]. Without nonlocality,  $\gamma$  can be expressed as a function  $\gamma(r_{\parallel}, r'_{\parallel}) = f(r_{\parallel}, r'_{\parallel}, t_d(r'_{\parallel}))$ . Inserting the first order Taylor expansion of  $f$  with respect

to  $t_d$  into Eq. 3 and dividing by  $\alpha_0$  yields the desired relation in which  $\alpha_{\text{rel}}$  is a convolution of  $t_d$  with a point spread function  $\gamma_{\text{topo}} = \partial f / \partial t_d \big|_{t_d=0}$ .

$$\alpha_{\text{rel}}(r_{\parallel}) = \frac{1}{\alpha_0} \iint_{\text{sample}} f(r_{\parallel}, r'_{\parallel}, 0) d^2 r'_{\parallel} + \frac{1}{\alpha_0} \iint_{\text{sample}} \gamma_{\text{topo}}(r_{\parallel}, r'_{\parallel}) t_d(r'_{\parallel}) d^2 r'_{\parallel}.$$

Since  $f(r_{\parallel}, r'_{\parallel}, 0)$  corresponds to  $\gamma$  in the absence of any topography  $t_d$ , the first integral equals  $\alpha_0$  and the first term is therefore simply one. We can obtain the shape of  $\gamma_{\text{topo}}$  from the consideration that a local topographic feature (that is, a small polarizable object) in the homogeneous field above the otherwise flat sample (Taylor expansion of  $f$ ) represents nothing else but a local dipole with a moment proportional to  $V_b$ . Hence, the contribution of such a feature to  $\alpha$  is similar to that of an actual dipole to  $\Phi_{\text{QD}}$ . Therefore,  $\gamma_{\text{topo}}$  has the same shape as  $\gamma_{\text{pp}}^*$  ( $\gamma_{\text{topo}} \propto \gamma_{\text{pp}}^*$ ), which is fully borne out by a finite element simulation [29]. The norm of  $\gamma_{\text{topo}}$  is found by using a calibration function  $g \approx (\alpha_{\text{rel}}(z + \Delta z) - \alpha_{\text{rel}}(z)) / \Delta z$  which is experimentally obtained by varying  $z$  by  $\Delta z$ . Typical experimental values are in the range of  $g \approx 0.03 \text{ \AA}^{-1}$ .

#### Data acquisition: from $V^{\pm}$ to $V^*$ and $\alpha_{\text{rel}}$

The  $V^+$  and  $V^-$  images of the same sample area are recorded consecutively ("2 pass") in constant height mode, typically at tip heights between 20 and 30  $\text{\AA}$  using the STC or ESC discussed above. To determine the calibration curve  $\alpha_{\text{rel}} = g \times (z - t)$  at the chosen QD height  $z$  which is required for the correct normalization of  $\gamma_{\text{topo}}$ , we measure  $V_0^{\pm}$  at one point of the reference area at heights  $z$  and  $z + 1 \text{ \AA}$ . This allows a linear estimate of  $\alpha_{\text{rel}}(z) = 1 + \alpha(z) \times t$  which is sufficiently accurate if the maximum of  $t$  is  $t_{\text{max}} \ll z$ . After recording the  $V^{\pm}$  images, standard image correction procedures like linear drift correction are applied if necessary. Finally, the  $V^*$  and  $\alpha_{\text{rel}}$  images are computed from the  $V^{\pm}$  images via Eqs. 5 and 6. For this procedure, a reference  $V_0^{\pm}$  is chosen on an empty part of the metal substrate.

#### Deconvolution

For the deconvolution of  $V^*$  we calculate the PSF  $\gamma^*(|r_{\parallel} - r'_{\parallel}|, z)$ . To be suitable for deconvolution on an  $m \times n$  image, the PSF is stored as a  $k \times k$  kernel matrix  $\mathbf{K}$  with  $k = 2l + 1$  where  $k$  and  $l$  are integers. To enable a correct treatment of pixels close to image borders, we expand the (deconvolved) image to a size of  $(m + 2l) \times (n + 2l)$  by adding  $l$  rows or columns on each side of the original image. Rows of  $\mathbf{K}$  correspond to the  $x$  component of  $|r_{\parallel} - r'_{\parallel}|$ , columns to the  $y$  component. Note that the value of matrix elements in  $\mathbf{K}$  only depends on the distance  $|r_{\parallel} - r'_{\parallel}|$ . The kernel matrix always has the same mesh size as the SQDM  $V^*$  and  $\alpha_{\text{rel}}$  images to be deconvolved (here typically 1-3  $\text{\AA}/\text{pixel}$ ). The sum over all  $k^2$  kernel matrix elements is normalized to 1 as required for  $\gamma^*$ . The size  $k$  of the kernel matrix is chosen such that the values at its edges are sufficiently close to zero ( $\mathbf{K}_{0l} \lesssim 5 \times 10^{-5} \mathbf{K}_{ll}$ ). Due to the exponential decay of the PSF with lateral distance this is the case already for kernels that measure only  $150 \times 150 \text{ \AA}^2$ . The elements of  $\mathbf{K}(|r_{\parallel} - r'_{\parallel}|, z)$  are

computed via the image charge method as discussed in the text (Fig. 2c). We use a point charge placed 1 Å above the surface and 100,000 image charges, which results in a full convergence of the potential between the tip and surface planes in the relevant lateral distance range. The matrix elements are then calculated as the lateral potential distribution  $d = 7$  Å beneath the tip plane [24].

Since SQDM scans are constant height scans, the effective QD-sample separation  $z - t_d(r_{||})$  varies with  $t_d$ , which, in turn, leads to variations of the actual PSF (cf. Eq. 7). As one consequence, identical nanostructures on substrate terraces of different height will not show the same  $V^*$  image contrast. We compensate this effect during deconvolution by dynamically adjusting the PSF to the local  $t_d(r_{||})$  value. To allow this, we calculate an entire set of  $\mathbf{K}$  matrices for a range of tip-surface distances. We assume a locally planar surface of height  $t_d$  which can then be obtained by inverting the relation  $\alpha_{\text{rel}} = 1 + g t_d$  with a value for  $g$  given above. This  $t_d(r_{||}) = (\alpha_{\text{rel}}(r_{||}) - 1)/g$  is then used with the given  $z$  to select the correct  $\mathbf{K}$  for each pixel in the  $V^*$  image. Thus, we retain the model of a planar sample surface for which  $\gamma^*$  can be easily computed and has axial symmetry, but we appropriately adjust the separation between both planes when determining the PSF for each pixel. A rigorous derivation of the underlying formalism is given elsewhere [29].

We deconvolve  $V^*$  and  $\alpha_{\text{rel}}$  images using an iterative non-linear deconvolution algorithm with a Tikhonov-Phillips regularization term to suppress over-amplification of noise and other deconvolution artefacts. We found in empirical tests that for our SQDM images, regularization based on the  $L_2$  norm (like Tikhonov-Phillips) leads to better results than regularization using the  $L_1$  norm (like the popular total variation minimization approach). To apply the Tikhonov-Phillips regularization we modify the expression for  $\chi^2$  and add a term that measures the squared variation between neighbouring pixels in the deconvolved image as

$$\chi^2 = \sum_{i=1}^m \sum_{j=1}^n (P_{ij}^{\text{exp}} - P_{ij}^{\text{conv}})^2 + \lambda \left[ (P_{ij} - P_{(i+1)j})^2 + (P_{ij} - P_{i(j+1)})^2 \right].$$

We have found that good deconvolution results are obtained with a value of  $\lambda = 0.0036/s^2$ , where  $s$  measures the image resolution in Å/pixel. This scaling is applied to enable deconvolution results that are independent of image resolution, since images with higher resolution are automatically smoother on a pixel-by-pixel level.

## Supplementary Material

Refer to Web version on PubMed Central for supplementary material.

## Acknowledgements

C.W. acknowledges funding through the European Research Council (ERC-StG 757634 "CM3"). A.T. and N.F. acknowledge funding by DFG-SFB 951 (project A10).

## References

- [1]. He Z, et al. Enhanced power-conversion efficiency in polymer solar cells using an inverted device structure. *Nature Photonics*. 2012; 6:593–597. DOI: 10.1038/nphoton.2012.190
- [2]. Tung RT. The physics and chemistry of the Schottky barrier height. *Applied Physics Reviews*. 2014; 1doi: 10.1063/1.4858400
- [3]. Chuang C-HM, Brown PR, Bulovi V, Bawendi MG. Improved performance and stability in quantum dot solar cells through band alignment engineering. *Nature Materials*. 2014; 13:796–801. DOI: 10.1038/nmat3984 [PubMed: 24859641]
- [4]. Fuchs F, Caffy F, Demadrille R, Mélin T, Grévin B. High-resolution Kelvin probe force microscopy imaging of interface dipoles and photogenerated charges in organic donor-acceptor photovoltaic blends. *ACS Nano*. 2016; 10:739–746. DOI: 10.1021/acsnano.5b05810 [PubMed: 26750993]
- [5]. Courtland R. Moore's law's next step: 10 nanometers. *IEEE Spectrum*. 2017; 54:52–53.
- [6]. Fuechsle M, et al. A single-atom transistor. *Nature Nanotechnology*. 2012; 7:242–246.
- [7]. Lin J, et al. Flexible metallic nanowires with self-adaptive contacts to semiconducting transition-metal dichalcogenide monolayers. *Nature Nanotechnology*. 2014; 9:436–442. DOI: 10.1038/nnano.2014.81
- [8]. Xiang D, Wang X, Jia C, Lee T, Guo X. Molecular-Scale Electronics: From Concept to Function. *Chemical Reviews*. 2016; 116:4318–4440. DOI: 10.1021/acs.chemrev.5b00680 [PubMed: 26979510]
- [9]. de Boer B, Hadipour A, Mandoc MM, van Woudenberg T, Blom PWM. Tuning of metal work functions with self-assembled monolayers. *Advanced Materials*. 2005; 17:621–625. DOI: 10.1002/adma.200401216
- [10]. Watson JD, Crick FHC. Molecular structure of nucleic acids. *Nature*. 1953; 171:737–738. [PubMed: 13054692]
- [11]. Moreira IS, Fernandes PA, Ramos MJ. Hot spots A review of the protein-protein interface determinant amino-acid residues. *Proteins*. 2007; 86:803–812. DOI: 10.1002/prot.21396
- [12]. Warshel A, et al. Electrostatic basis for enzyme catalysis. *Chemical Reviews*. 2006; 106:3210–3235. DOI: 10.1021/cr0503106 [PubMed: 16895325]
- [13]. Zerweck U, Loppacher C, Otto T, Grafström S, Eng LM. Accuracy and resolution limits of Kelvin probe force microscopy. *Physical Review B*. 2005; 71doi: 10.1103/PhysRevB.71.125424
- [14]. Baier R, Leendertz C, Lux-Steiner MC, Sadewasser S. Toward quantitative Kelvin probe force microscopy of nanoscale potential distributions. *Physical Review B*. 2012; 85doi: 10.1103/PhysRevB.85.165436
- [15]. Musumeci C, Liscio A, Palermo V, Samorì P. Electronic characterization of supramolecular materials at the nanoscale by Conductive Atomic Force and Kelvin Probe Force microscopies. *Materials Today*. 2014; 17:504–517.
- [16]. Söngen H, et al. The weight function for charges - A rigorous theoretical concept for Kelvin probe force microscopy. *Journal of Applied Physics*. 2016; 119doi: 10.1063/1.4939619
- [17]. Gross L, et al. Measuring the charge state of an adatom with noncontact atomic force microscopy. *Science*. 2009; 324:1428–1431. [PubMed: 19520956]
- [18]. Sadewasser S, et al. New insights on atomic-Resolution frequency-Modulation kelvin-Probe force-Microscopy imaging of semiconductors. *Physical Review Letters*. 2009; 103doi: 10.1103/PhysRevLett.103.266103
- [19]. Schuler B, et al. Contrast Formation in Kelvin Probe Force Microscopy of Single pi-Conjugated Molecules. *Nano letters*. 2014; 14:3342–3346. DOI: 10.1021/nl500805x [PubMed: 24849457]
- [20]. Albrecht F, et al. Probing Charges on the Atomic Scale by Means of Atomic Force Microscopy. *Physical Review Letters*. 2015; 115doi: 10.1103/PhysRevLett.115.076101
- [21]. Hapala P, et al. Mapping the electrostatic force of single molecules from high-resolution scanning probe images. *Nature communications*. 2016
- [22]. Fournier N, Wagner C, Weiss C, Temirov R, Tautz FS. Force-controlled lifting of molecular wires. *Physical Review B*. 2011; 84doi: 10.1103/PhysRevB.84.035435

- [23]. Wagner C, Fournier N, Tautz FS, Temirov R. Measurement of the binding energies of the organic-metal perylene-teracarboxylic-dianhydride/Au(111) bonds by molecular manipulation using an atomic force microscope. *Physical Review Letters*. 2012; 109doi: 10.1103/PhysRevLett.109.076102
- [24]. Wagner C, et al. Scanning Quantum Dot Microscopy. *Physical Review Letters*. 2015; 115doi: 10.1103/PhysRevLett.115.026101
- [25]. Green MFB, et al. Scanning quantum dot microscopy : A quantitative method to measure local electrostatic potential near surfaces. *Japanese Journal of Applied Physics*. 2016; 55doi: 10.7567/JJAP.55.08NA04
- [26]. Maiworm, M; Wagner, C; Temirov, R; Tautz, FS; Findeisen, R. Two-degree-of-freedom control combining machine learning and extremum seeking for fast scanning quantum dot microscopy. American Control Conference (ACC); Milwaukee, WI, USA. USA: IEEE; 2018. 4360–4366. URL <https://ieeexplore.ieee.org/abstract/document/8431022>
- [27]. Likharev K. Single-electron devices and their applications. *Proceedings of the IEEE*. 1999; 87:606–632.
- [28]. Jackson, JD. *Classical electrodynamics*. 3 edn. Wiley; New York: 1999.
- [29]. Wagner C, Tautz FS. *The theory of scanning quantum dot microscopy*.
- [30]. Stomp R, et al. Detection of Single-Electron Charging in an Individual InAs Quantum Dot by Noncontact Atomic-Force Microscopy. *Physical Review Letters*. 2005; 94doi: 10.1103/PhysRevLett.94.056802
- [31]. Miyahara Y, Roy-Gobeil A, Grutter P. Quantum state readout of individual quantum dots by electrostatic force detection. *Nanotechnology*. 2017; 28doi: 10.1088/1361-6528/aa5261/meta
- [32]. Temirov R, et al. Molecular Model of a Quantum Dot Beyond the Constant Interaction Approximation. *Physical Review Letters*. 2018; 120doi: 10.1103/PhysRevLett.120.206801
- [33]. Tautz FS. Structure and bonding of large aromatic molecules on noble metal surfaces: The example of PTCDA. *Progress in Surface Science*. 2007; 82:479–520.
- [34]. Zou Y, et al. Chemical bonding of PTCDA on Ag surfaces and the formation of interface states. *Surface Science*. 2006; 600:1240–1251.
- [35]. Kawabe E, et al. A role of metal d-band in the interfacial electronic structure at organic/metal interface: PTCDA on Au, Ag and Cu. *Organic Electronics*. 2008; 9:783–789.
- [36]. Duhm S, et al. PTCDA on Au(111), Ag(111) and Cu(111): Correlation of interface charge transfer to bonding distance. *Organic Electronics*. 2008; 9:111–118.
- [37]. Ferri N, DiStasio RA Jr, Ambrosetti A, Car R, Tkatchenko A. Electronic Properties of Molecules and Surfaces with a Self-Consistent Interatomic van der Waals Density Functional. *Physical Review Letters*. 2015; 114doi: 10.1103/PhysRevLett.114.176802
- [38]. Ruiz VG, Liu W, Zojer E, Scheffler M, Tkatchenko A. Density-Functional Theory with Screened vanderWaals Interactions for the Modeling of Hybrid Inorganic-Organic Systems. *Physical Review Letters*. 2012; 108doi: 10.1103/PhysRevLett.108.146103
- [39]. Perdew JP, Burke K, Ernzerhof M. Generalized gradient approximation made simple. *Physical Review Letters*. 1996; 77:3865–3868. DOI: 10.1103/PhysRevLett.77.3865 [PubMed: 10062328]
- [40]. Kellogg, OD. *Foundations of Potential Theory*. Springer; Berlin: 1929.
- [41]. Pumplin J. Application of Sommerfeld-Watson Transformation to an Electrostatics Problem. *American Journal of Physics*. 1969; 37:737.doi: 10.1119/1.1975793
- [42]. Lan F, Jiang M, Tao Q, Wei F, Li G. Reconstruction of Kelvin probe force microscopy image with experimentally calibrated point spread function. *Review of Scientific Instruments*. 2017; 88doi: 10.1063/1.4978282
- [43]. Esat T, Friedrich N, Tautz FS, Temirov R. A standing molecule as a single-electron field emitter. *Nature*. 2018; 558:573. [PubMed: 29950622]
- [44]. Schulman JH, Hughes AH. On the surface potentials of unimolecular films. Part IV. - The effect of the underlying solution and transition phenomena in the film. *Proceedings of the Royal Society of London*. 1932; 138:430–450.
- [45]. Gross L, Mohn F, Moll N, Liljeroth P, Meyer G. The chemical structure of a molecule resolved by atomic force microscopy. *Science*. 2009; 325:1110–4. [PubMed: 19713523]



- [46]. Wagner C, Temirov R. Tunnelling junctions with additional degrees of freedom: An extended toolbox of scanning probe microscopy. *Progress in Surface Science*. 2015; 90:194–222.
- [47]. Schneiderbauer M, Emmrich M, Weymouth AJ, Giessibl FJ. CO Tip Functionalization Inverts Atomic Force Microscopy Contrast via Short-Range Electrostatic Forces. *Physical Review Letters*. 2014; 112doi: 10.1103/PhysRevLett.112.166102
- [48]. Schwarz A, Köhler A, Grenz J, Wiesendanger R. Detecting the dipole moment of a single carbon monoxide molecule. *Applied Physics Letters*. 2014; 105doi: 10.1063/1.4890324
- [49]. van der Lit J, Di Cicco F, Hapala P, Jelinek P, Swart I. Submolecular Resolution Imaging of Molecules by Atomic Force Microscopy: The Influence of the Electrostatic Force. *Physical Review Letters*. 2016; 116doi: 10.1103/PhysRevLett.116.096102
- [50]. Feibelman PJ, et al. The CO/Pt(111) Puzzle. *The Journal of Physical Chemistry B*. 2001; 105:4018–4025. DOI: 10.1021/jp002302t
- [51]. Ren X, Rinke P, Scheffler M. Exploring the random phase approximation: Application to CO adsorbed on Cu(111). *Physical Review B*. 2009; 80doi: 10.1103/PhysRevB.80.045402
- [52]. Kraft A, et al. Lateral adsorption geometry and site-specific electronic structure of a large organic chemisorbate on a metal surface. *Physical Review B*. 2006; 74doi: 10.1103/PhysRevB.74.041402
- [53]. Willenbockel M, et al. The interplay between interface structure, energy level alignment and chemical bonding strength at organic-metal interfaces. *Physical Chemistry Chemical Physics*. 2015; 17:1530.doi: 10.1039/c4cp04595e [PubMed: 25475998]
- [54]. Repp J, Meyer G, Rieder KH. Snell's Law for Surface Electrons: Refraction of an Electron Gas Imaged in Real Space. *Physical Review Letters*. 2004; 92doi: 10.1103/PhysRevLett.92.036803
- [55]. Ariyur, KB, Krsti , M. *Real-Time Optimization by Extremum-Seeking Control*. Wiley & Sons; Hoboken, New Jersey: 2003.



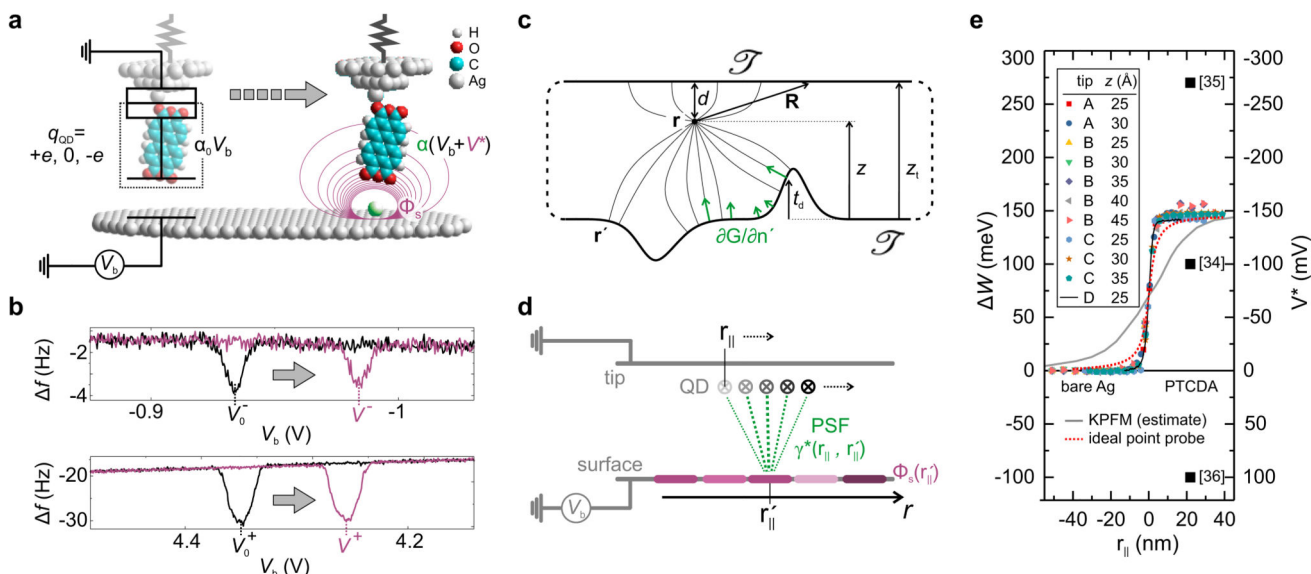


### Figure 1. Principle and quantitative nature of SQDM

**a**, Principle of electric potential sensing with a molecular QD. When placed above a bare surface, the QD changes its charge by  $\pm e$  if its potential  $\Phi_{\text{QD}} = \alpha_0 V_b$  reaches the threshold values  $\Phi^\pm$  at  $V_b = V_0^\pm$ . The local topography (green) and the surface potential  $\Phi_s$  (violet) of a nanostructure (here: adatom) change the QD potential  $\Phi_{\text{QD}}$ , as  $\alpha_0$  changes to  $\alpha$  and  $V^*$  is added to  $V_b$ . In the equivalent circuit diagram superimposed on the left, the QD is marked by a dashed box. **b**,  $f(V_b) = -dF_z/dz \times f_0/(2k_0)$  curves (qPlus type NC-AFM with  $k_0 = 1800$  N/m,  $f_0 = 31200$  Hz, amplitude  $A = 0.2$  Å) in the  $V_b$  ranges where the QD changes its charge state (upper panel  $V^-$ , lower panel  $V^+$ ), measured above the empty surface (black) and above a nanostructure (violet). The change from  $\alpha_0$  to  $\alpha$  and the additional contribution  $V^*$  (see Panel a) leads to a shift from  $V_0^\pm$  to  $V^\pm$ . **c**, Illustration of SQDM as a boundary value problem with the QD at  $r$ . Tip and surface are connected at infinity. **d**, The PSF  $\gamma^*$  describes the contribution of the potential  $\Phi_s(r_{\parallel})$  (shades of violet illustrate magnitude) to  $\Phi_{\text{QD}}$  at all possible positions  $r_{\parallel}$  (visualized by green lines). For flat surfaces, reciprocally,  $\Phi_{\text{QD}}$  at a certain lateral position  $r_{\parallel}$  is the sum over all local potentials on the sample surface at positions  $r'_{\parallel}$  weighted with  $\gamma^*$ . **e**, Series of  $V^*$  profiles across a PTCDA/Ag(111) island edge measured with different tips and tip heights as indicated. The expected profiles for corresponding measurements with KPFM [13] and with an ideal point probe ( $z = 25$  Å) are shown for comparison. The measured work function change for a PTCDA layer corresponds to  $W = -eV^*$  at positive  $r_{\parallel}$ . Values for  $W$  reported in literature are indicated as black squares.

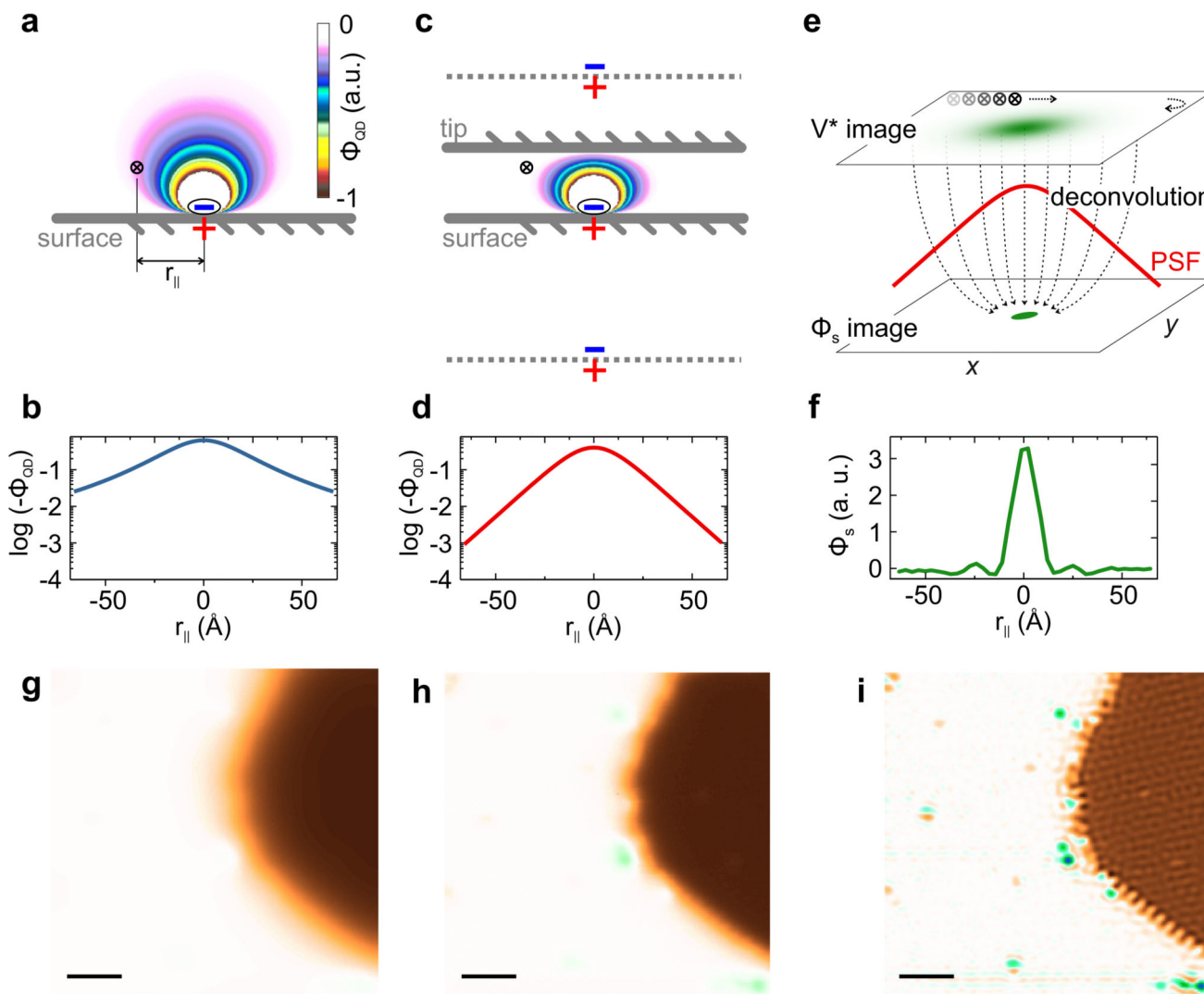


**Figure 2. Electrostatic screening and image deconvolution in SQDM**

**a**, Simulated potential  $\Phi_{\text{QD}}$  above a charge/image-charge dipole on a conductive surface. A point-like potential probe at a lateral distance  $r_{\parallel}$  is indicated by a cross. **b**, Cross-section through the potential  $\Phi_{\text{QD}}$  at the height of the point probe in Panel a. **c**, Same as in Panel a, but with a second conductive plane ("tip") above the point probe. The potential distribution can now be simulated via an infinite series of image dipoles. Two images are indicated as dashed lines. The potential  $\Phi_{\text{QD}}$  at the point probe position is reduced compared to Panel a. **d**, Cross-section through the potential  $\Phi_{\text{QD}}$  at the height of the probe in Panel c. The log-scale plot reveals the exponential decay of  $\Phi_{\text{QD}}$  with lateral distance from the dipole. **e**, Illustration of the deconvolution process in which the  $\Phi_{\text{s}}$  image is recovered from the measured  $V^*$  image using  $\Phi_{\text{QD}}(r_{\parallel})$  from Panel d as the PSF  $\gamma^*$ . **f**, Cross-section through the  $\Phi_{\text{s}}$  image of a CO molecule on Ag(111) as obtained from deconvolution. The full width at half maximum is only 1.6 nm. **g**, Simulation of an SQDM  $V^*$  image for the hypothetical setup without a tip (Panel a). Simulation based on the image in Panel i. **h**, Measured SQDM  $V^*$  image (STC controller) of a complex surface with extended PTCDA islands and smaller

nanostructures (compare Fig. 3). **i**, SQDM  $\Phi_s$  image as obtained from the  $V^*$  image in Panel h via deconvolution (see Methods). All nanostructures are now equally well visible. The scale bar size in Panels g-i is 10 nm.

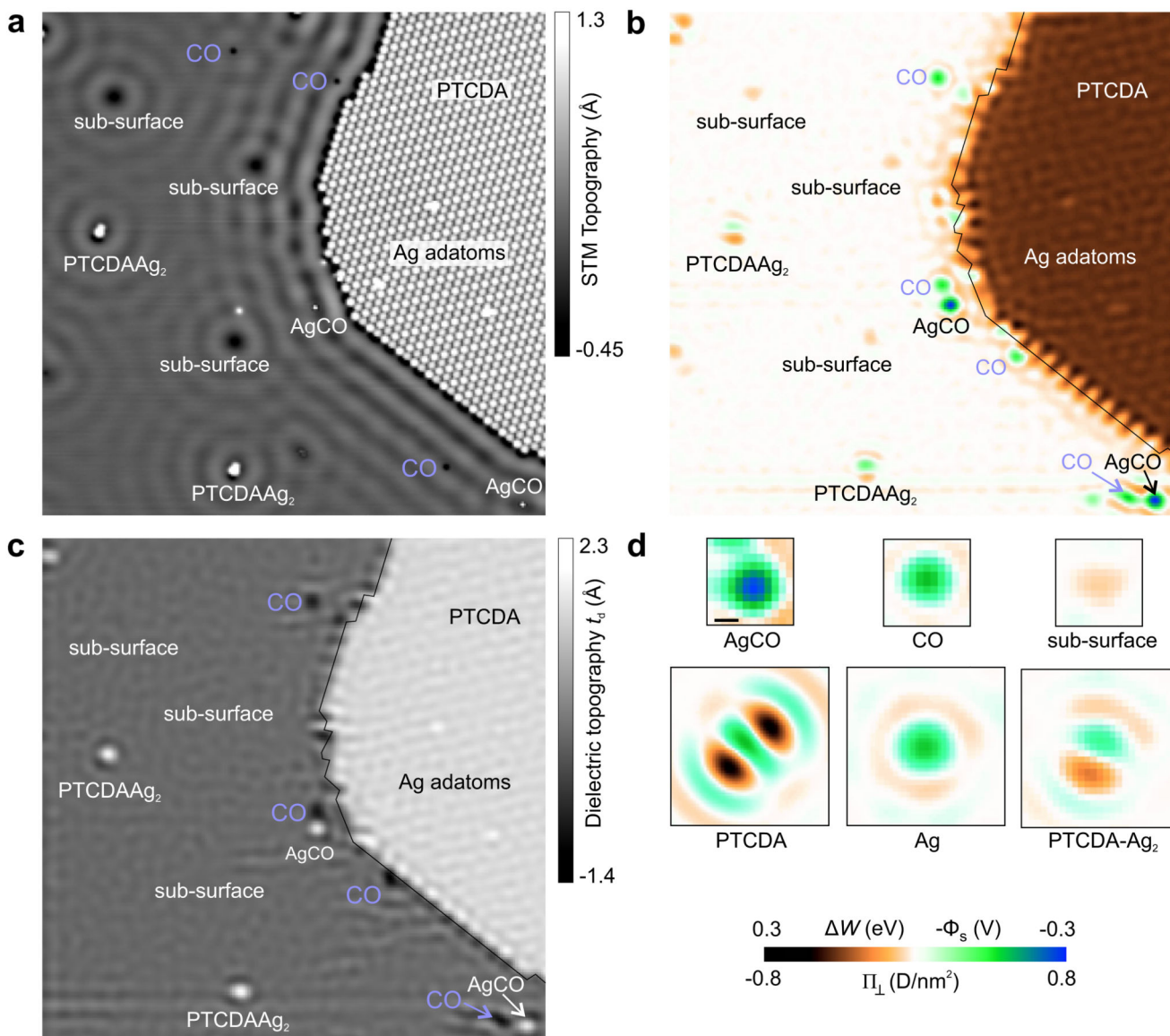


**Figure 3. SQDM images of nanostructures on Ag(111)**

Image size for a-c is  $60 \times 60 \text{ nm}^2$ . **a**, STM image ( $V_b = 20 \text{ mV}$ ) showing various adsorbates and defects on a Ag(111) surface. **b**, SQDM  $\Phi_s$  image (STC controller) of the area in Panel a. All features from Panel a are visible, however, the mobile CO molecules have moved to different locations. The thin black line traces the PTCDA island edge from Panel a. The rows of inequivalent PTCDA molecules on the island edges and within the island are resolved. See Supplementary Information for corresponding  $V^{\pm}$  images. **c**, SQDM dielectric topography image of the area in Panel a. The absolute scale  $t_q$  is obtained from calibration measurements of  $a_{\text{rel}}(z)$ . The subsurface defects do not exhibit any topographic feature. **d**, Cutouts from several SQDM  $\Phi_s$  images of individual nanostructures including a PTCDA-Ag<sub>2</sub> complex [43]. The colour scale refers to Panels b and d. The scale bar in d is 1 nm.

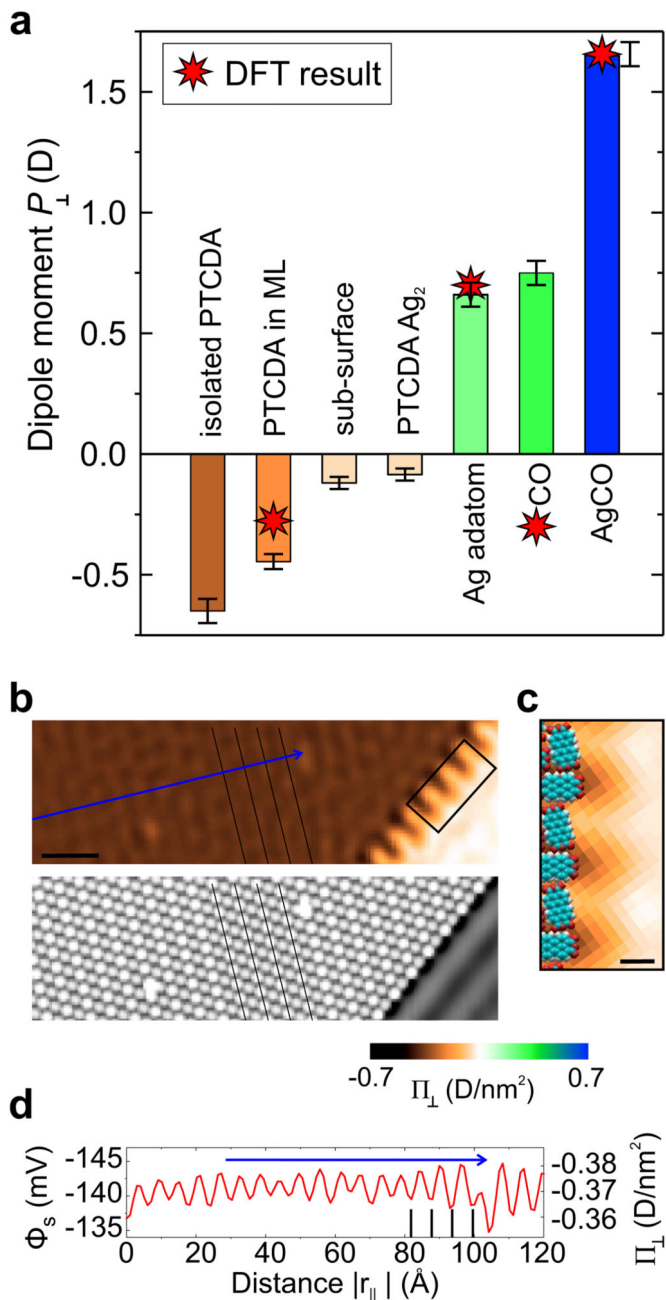


**Figure 4. Surface dipoles of selected nanostructures and dipole density within a layer.**  
**a**, Surface dipole moments of adatoms, molecules or complexes with indicated error bars and DFT simulation results. The error bars approximate the uncertainty due to fringing artefacts in the deconvolved images. **b**, Cutout STM (bottom) and SQDM  $\Phi_s$  image (top) from Fig. 3. Black lines indicate adjacent rows of identically adsorbed PTCDA molecules. The scale bar is 5 nm. **c** Zoom of the island border region marked in Panel b. The orientation and size of PTCDA molecules at the border is indicated. The scale bar is 1 nm. **d** The line profile through the  $\Phi_s$  image along the blue arrow in Panel b reveals a modulation caused by

rows of inequivalent PTCDA molecules. Black vertical lines correspond to the rows marked in Panel b.